

Stabilization and modulation of the topological magnetic phase with a Z_2 -vortex lattice in the Kitaev-Heisenberg honeycomb model: The key role of the third-nearest-neighbor interaction

Xiaoyan Yao* and Shuai Dong†

School of Physics, Southeast University, Nanjing 211189, China

[Abstract] The topologically nontrivial magnetic phase with a Z_2 -vortex (Z_2V) lattice is investigated by simulation in the Kitaev-Heisenberg honeycomb model expanded by considering the second- and third-nearest-neighbor Heisenberg interactions (J_{H2} and J_{H3}). On the parameter region of the Z_2V phase, a gradual modulation of vortex density is observed, together with a transition from single- Z_2V to triple- Z_2V state driven by the variation of frustration. Additionally, Z_2 vortices are arranged in different manners on the whole honeycomb structure for these two types of Z_2V states. Moreover, topologically equivalent states are revealed to exist in single- Z_2V dominant and triple- Z_2V dominant styles on different parameter points, which can be controlled to switch between each other without energy consumption. It is worth noting that J_{H3} plays a key role in expanding the Z_2V phase, and also in stabilizing the single- Z_2V state.

* Corresponding author: yaoxiaoyan@seu.edu.cn

† Corresponding author: sdong@seu.edu.cn

I. INTRODUCTION

Vortices have long been a hot topic in many fields of physics research, and are believed to be associated with various intriguing phenomena, such as Abrikosov vortices in type-II superconductors [1, 2] and the vortex domains in multiferroic hexagonal manganites [3-7]. It is well known that the topological Z vortices characterized by the integral winding number Z could appear in a two-dimensional system where the order-parameter space is the two-dimensional rotation group $SO(2)$ or the one-dimensional circle S_1 [$SO(2)=S_1$]. The Kosterlitz-Thouless transition in a XY ferromagnet is driven by the dissociation of Z vortices [8, 9]. If the ferromagnet is considered to be Heisenberg type, the Z vortex will be topologically trivial because the order-parameter space is the two-dimensional sphere S_2 . Since there is no topological point defect, no topological phase transition takes place. However, the frustration could bring another type of topological defect into Heisenberg spin systems. When the order-parameter space is the three-dimensional rotation group $SO(3)$ or the projective space P_3 [$SO(3)=P_3$] as shown in the frustrated triangular Heisenberg antiferromagnet, a Z_2 vortex (Z_2V) characterized by the two-valued topological quantum number emerges. Here, the ground state is the 120° spin structure with 120° between every two nearest-neighbor spins on the triangular lattice. The order parameter is not one spin, but a rigid rotator consisting of three spins on an elementary triangle [10]. These rotators circulate around a core making a topologically stable vortex. Two Z_2 vortices (Z_2Vs) can annihilate each other. Whether they circulate in clockwise or counterclockwise fashion makes no difference topologically. The binding-unbinding of these thermally excited Z_2Vs drives the thermodynamic phase transition at a finite temperature without conventional long-range order in these systems [10-13].

Since the unconventional bond-dependent Kitaev coupling was believed to be substantial in the hexagonal iridates $A_2\text{IrO}_3$ ($A = \text{Na}, \text{Li}$), the Kitaev-Heisenberg (KH) model attracted considerable attention, and had been proposed to capture the essential magnetic interactions in these iridates [14-22]. Recently, $\alpha\text{-RuCl}_3$ was also suggested as a candidate Kitaev material in a $4d$ analog of honeycomb iridates [23-30]. The unconventional Kitaev interaction breaks the spin rotational symmetry and provides an avenue for a new kind of frustration, namely, the Kitaev frustration. As the geometrical frustration is introduced, the region with puzzled magnetic states was observed on the phase diagram [31, 32]. Recently, the topological Z_2Vs , not thermally excited, were observed in the triangular KH model. The Kitaev term in the exchange Hamiltonian condenses these vortices into a Z_2V crystal at zero temperature [33, 34]. In addition, our previous report explored a wide parameter range of the KH honeycomb model with the next-nearest-neighbor Heisenberg interaction considered, and found an inhomogeneous state exhibiting a topological triple-vortex lattice. But this triple- Z_2V state only exists on the phase boundaries [35]. Its existing region of the ground state is too narrow to be well located, and thus it will be too hard to be observed in experiments.

The present paper focuses on the topological Z_2V phase in the KH honeycomb model expanded by considering further neighboring interactions. The existing range of the Z_2V ground state is carefully confirmed by detailed analyses, and it is revealed to be effectively expanded by the third-nearest-neighbor Heisenberg interaction with appropriate magnitude. In the Z_2V phase area, a nearly continuous modulation of vortex density is observed, resulting

from a continuous modulation on spin configurations. Furthermore, a transition from single- Z_2V to triple- Z_2V state is revealed to be induced by the variation of mixed frustration, and the third-nearest-neighbor Heisenberg interaction plays a key role in stabilizing the single- Z_2V state. The topologically equivalent states could exist in single- Z_2V dominant and triple- Z_2V dominant fashions on different parameter points, which can be controlled to switch between each other without energy consumption. Moreover, the simulation shows that the Z_2V s are arranged in different styles on the honeycomb structure for the single- Z_2V and triple- Z_2V states.

II. METHODS

Considering the expanded KH model where J_K is the Kitaev interaction coupling different spin components (S^x , S^y , and S^z) on the nearest-neighbor bonds along the three lattice directions labeled by $\gamma=xx$, yy and zz as presented in Fig. 1(a). J_H , J_{H2} , and J_{H3} represent the isotropic Heisenberg couplings between spins on the nearest-neighbor ($\langle i, j \rangle$), the second-nearest-neighbor ($\langle\langle i, k \rangle\rangle$), and the third-nearest-neighbor ($\langle\langle\langle i, l \rangle\rangle\rangle$) sites. The Hamiltonian takes the form of

$$H = J_K \sum_{\langle i, j \rangle_\gamma} S_i^\gamma \cdot S_j^\gamma + J_H \sum_{\langle i, j \rangle} \mathbf{S}_i \cdot \mathbf{S}_j + J_{H2} \sum_{\langle\langle i, k \rangle\rangle} \mathbf{S}_i \cdot \mathbf{S}_k + J_{H3} \sum_{\langle\langle\langle i, l \rangle\rangle\rangle} \mathbf{S}_i \cdot \mathbf{S}_l. \quad (1)$$

$\sqrt{J_H^2 + J_K^2} = 1$ is fixed as the energy scale. We consider the region of antiferromagnetic (AFM) $J_H > 0$ and ferromagnetic $J_K < 0$ as originally proposed for the KH model relevant to iridates [14, 15]. Then the ratio of J_H to J_K is considered by parametrizing $J_H = \cos\varphi$ and $J_K = \sin\varphi$ with $\varphi: 1.5\pi \sim 2\pi$. Monte Carlo (MC) simulation of the Metropolis algorithm combined with the over-relaxation method is performed on the honeycomb lattice of $N=9216$ sites with periodic boundary conditions assumed [36, 37]. On every parameter point, the system is first evolved from a relatively high temperature (T) near 1 to a very low $T=0.0000001$ gradually, and then the energy is further minimized by 100000 MC steps restricted at $T=0$ (namely, only the proposed update with the energy variation not higher than zero is accepted) to approach the limit of zero temperature. The final result is obtained by comparing independent data sets evolving from different initial states.

The states obtained from MC simulation can be preliminarily distinguished by the spin correlations as calculated by

$$\begin{aligned} C_n &= \langle \mathbf{S}_i \cdot \mathbf{S}_{i+1} \rangle_n \\ C_{nn} &= \langle \mathbf{S}_i \cdot \mathbf{S}_{i+2} \rangle_{nn} \\ C_{nnn} &= \langle \mathbf{S}_i \cdot \mathbf{S}_{i+3} \rangle_{nnn} \\ C_K &= \langle S_i^x \cdot S_{i+1}^x \rangle_{xx} + \langle S_i^y \cdot S_{i+1}^y \rangle_{yy} + \langle S_i^z \cdot S_{i+1}^z \rangle_{zz} \end{aligned}, \quad (2)$$

where C_n , C_{nn} , and C_{nnn} are spin correlations on the nearest-neighbor, the second-nearest-neighbor, and the third-nearest-neighbor spin pairs. C_K is the spin correlation of the nearest-neighbor Kitaev bonds. Five well-known commensurate ordered phases—ferromagnetic (F), Neel (N), stripy (S), zigzag (Z) and double 120° (D) phases—are identified by comparing to the standard values of correlations listed in Table I with less than

15% deviation. Here D is a phase where both triangular sublattices show coplanar 120° spin structures. These phases are further confirmed by the spin structure factors [38, 39], which can be calculated on one triangular sublattice (TSL) of the honeycomb structure as follows:

$$S^\gamma(\mathbf{k}) = \sum_{i,j} e^{i\mathbf{k}\cdot(\mathbf{r}_j - \mathbf{r}_i)} \langle \mathbf{S}_i^\gamma \cdot \mathbf{S}_j^\gamma \rangle_{TSL} \quad (3)$$

$S^\gamma(\mathbf{k})$ is evaluated for three spin components ($\gamma=x, y,$ and z), respectively, to show the detailed spin structure induced by the anisotropic Kitaev interaction.

To distinguish the phase with Z_2 Vs from the unidentified region, further analysis is required. First, since Z_2 V is a topological defect of the 120° spin structure, the local 120° spin pattern with slight distortion is required. To measure it, the chirality vector ($\boldsymbol{\kappa}$) is calculated on the spin configuration of one TSL in the form of

$$\boldsymbol{\kappa}(r) = \frac{2}{3\sqrt{3}} (\mathbf{S}_1 \times \mathbf{S}_2 + \mathbf{S}_2 \times \mathbf{S}_3 + \mathbf{S}_3 \times \mathbf{S}_1), \quad (4)$$

where the subscripts 1, 2, and 3 number the corner sites clockwise around each elementary triangle [Fig. 1(a)]. The orientation of $\boldsymbol{\kappa}$ is perpendicular to the plane on which the local 120° spin pattern lies approximately. The magnitude of $\boldsymbol{\kappa}$ ($|\boldsymbol{\kappa}|$) gives a measure of the rigidity of the 120° pattern, and it is normalized to unity for a perfect one. Here the averaged magnitude of $\boldsymbol{\kappa}$ higher than 0.74 is set for the Z_2 V phase to ensure the 120° spin structure kept locally. Second, the typical feature of spin structure factor for the Z_2 V phase, where 12 main peaks for three spin components are separately located along the hexagon's edges, is checked [35]. Third, the vorticity (ν) is calculated on $\boldsymbol{\kappa}$ configuration in the same manner as Ref. [10] by going around the right- and left-pointing triangular loops as illustrated in Fig. 1(a). ν is rescaled to be zero for no rotation and 1 for a rotation by 2π . The sum of ν (VS) is counted, and its nonzero value finally confirms the Z_2 V phase. Following these steps, Z_2 V can be well located and measured. The simulation confirms that Z_2 V is actually the rotation of the local 120° pattern. As shown in Fig. 1(b), the calculated $\boldsymbol{\kappa}$ vectors form a typical vortex with the smallest $|\boldsymbol{\kappa}|$ as the vortex core. Correspondingly, the calculated ν map confirms a Z_2 V in the center as illustrated in Fig. 1(c). If two Z_2 V cores are counted in one loop, $\nu=0$ is obtained, implying the annihilation of these two Z_2 Vs.

To explore ground states, the averaged energies per site for the commensurate ordered F, N, S, Z, and D phases are estimated as follows:

$$\begin{aligned} E_F &= (3J_H + 6J_{H2} + 3J_{H3} + J_K) / 2 \\ E_N &= (-3J_H + 6J_{H2} - 3J_{H3} - J_K) / 2 \\ E_S &= (-J_H - 2J_{H2} + 3J_{H3} - |J_K|) / 2 \\ E_Z &= (J_H - 2J_{H2} - 3J_{H3} - |J_K|) / 2 \\ E_D &= (-3J_{H2} - |J_K|) / 2 \end{aligned} \quad (5)$$

Every state obtained from MC simulation is checked by comparing its energy (E_{MC}) to the above energies of commensurate phases to confirm the ground state. The energy of the metastable state is required to be not higher than the ground state by 0.005.

III. RESULTS AND DISCUSSION

The phase diagrams obtained by simulation indicate that J_{H2} and J_{H3} play important roles

in generating Z_2V phase. Figures 2(a)-2(d) plot the phase diagrams in the space of φ and J_{H2} with different J_{H3} . Without J_{H2} and J_{H3} , only S and N phases can be identified on the bottom line in Fig. 2(a), and the S phase is induced by Kitaev frustration. When the geometrical frustration is switched on by AFM J_{H2} , the D phase, which is the base to generate Z_2Vs , appears and spreads with J_{H2} increasing. The interaction between Kitaev frustration and geometrical frustration induces the Z_2V state appearing along the boundary between D and S phases, but its region as a ground state is too narrow as mentioned in Ref. [35] without J_{H3} . According to C_{nm} listed in Table I, the AFM J_{H3} enhances Z and N phases, while suppressing S and F phases. When J_{H3} is switched on, the Z phase spreads into this parameter region [Figs. 2(b-d)], and it is confirmed as the ground state for Na_2IrO_3 and $\alpha\text{-RuCl}_3$ [26, 27, 40-42]. At the same time, the obvious shrink of the S phase opens an interval between D and S phases, in which the Z_2V phase expands greatly, as shown in Fig. 2(b) with $J_{H3}=0.1$. As J_{H3} is increased to 0.15, the S phase nearly disappears and the Z_2V phase is further enhanced [Fig. 2(c)]. However, as J_{H3} is raised higher, the region of the Z_2V phase is suppressed and moved to higher φ and J_{H2} with the expansion of N and Z phases [Fig. 2(d)]. On the other hand, Figs. 2(e)-2(h) plot the phase diagrams in the space of φ and J_{H3} with different J_{H2} , where AFM J_{H2} enhances the D phase but suppresses the N phase according to C_{nm} listed in Table I. As J_{H2} increases, firstly the Z_2V phase spreads to some extent with the N phase shrinking, and then it is squeezed by too strong a D phase. In summary, the optimal parameter range of the Z_2V phase is about 0.3-0.5 for J_{H2} and 0.1-0.2 for J_{H3} . Besides J_{H2} , which brings geometrical frustration to produce the D phase, J_{H3} plays a key role in stabilizing the Z_2V phase on a larger parameter region. In addition, the metastable Z_2V state always appears in the ground-state region of the D phase to the left of the Z_2V ground state. As the topological point defects, Z_2Vs cannot be removed by small modifications, which makes them rather stable, existing in ground states and metastable states on the phase diagram of zero temperature.

In the whole region of the Z_2V phase in the phase diagrams of Fig. 2, all Z_2Vs are observed in the form of a Z_2V crystal. The vortex density increases with φ rising but decreases with J_{H2} or J_{H3} rising, presenting a nearly continuous modulation. Figure 3 illustrates two typical cases with $VS=1152$ and 72 , namely, a dense and a sparse Z_2V crystals. As shown in Fig. 3(a), $VS=1152$ is the densest Z_2V lattice that can be shown here, where Z_2Vs are closely packed in a Kagome lattice as presented in the $\nu(r)$ map. Higher VS exists, but it is too dense to be exactly located and exhibited by the present method. In the sparse case of $VS=72$ [Fig. 3(d)], Z_2Vs are separated far away from each other, forming a triangular lattice. In addition, $S^\gamma(\mathbf{k})$ shows the typical peaks as plotted in Figs. 3(b) and 3(e). As VS decreases, the main peaks of $S^\gamma(\mathbf{k})$ slide along the hexagon's edges from M to K points (M is the midpoint of the edge and K is the corner of the first Brillouin zone). The vortex comes from the superlattice of $\kappa(r)$, which can be better characterized by a Fourier transform, that is, the structure factor of $\kappa(r)$ [$S\kappa^\gamma(\mathbf{k})$] can be calculated by

$$S\kappa^\gamma(\mathbf{k}) = \sum_{i,j} e^{ik \cdot (r_j - r_i)} \langle \kappa_i^\gamma \cdot \kappa_j^\gamma \rangle_{\text{TSL}}, \quad (6)$$

where $S\kappa^\gamma(\mathbf{k})$ is also calculated for three components ($\gamma=x, y,$ and z), respectively. The main peaks of $S\kappa^\gamma(\mathbf{k})$ appear on the midperpendicular lines to the hexagon's edges, moving toward the center with decreasing VS , as shown in Figs. 3(c) and 3(f). If the wave vector of the $S^\gamma(\mathbf{k})$ main peak is denoted by \mathbf{k}_p and that of the $S\kappa^\gamma(\mathbf{k})$ main peak is denoted by $\mathbf{k}\mathbf{k}_p$, their averaged

magnitudes $|k_p|$ and $|kk_p|$ present a good correspondence to VS as plotted in Fig. 4(a). With VS rising, $|k_p|$ decreases while $|kk_p|$ increases gradually, showing that the continuous variation of vortex density results from the continuous modulation on $\kappa(r)$ and spin configuration.

It is interesting that the modulation of the Z_2V lattice is actually not a simple drifting apart. When VS is low, Z_2Vs exist in the single style as shown in Fig. 3(d). As VS increases, the aggregation of Z_2Vs prefers trimerization, and thus the triple- Z_2V state with three Z_2Vs combined together is observed as reported in the case without J_{H3} [35]. To detect this detail, the ratio of single vortices to all vortices (RS) is estimated. In the case of $J_{H3}=0$ [Fig. 2(a)], only the Z_2V states with RS near zero are displayed. When $J_{H3}=0.2$ [Fig. 2(d)], there are only the Z_2V states with RS=1. As $J_{H3}=0.1$ and 0.15 [Figs. 2(b) and 2(c)], RS presents a more abrupt transition than the continuous variation of VS, which is also seen in Figs. 2(e)-2(h). The jump of RS means a transition from the single- to triple- Z_2V state, and it happens at about $J_{H3}=0.1-0.15$. It is worth noting that the triple- Z_2V state always appears beside the S phase. If the S phase disappears completely, the triple- Z_2V state also vanishes as shown in Fig. 2(d). As plotted in Figs. 4(c)-4(f), from the single- Z_2V state near the D phase to the triple- Z_2V state close to the S phase on the Z_2V area, $|C_n|$ and $|C_{nn}|$ (correlations between two TSLs) increase, while $|C_{nn}|$ (correlation within one TSL) and $|\kappa|$ decrease. It is indicated that the single- Z_2V state with stronger intra-TSL correlation and weaker inter-TSL ones mostly results from the mixed frustration within one TSL, while the triple- Z_2V state is induced by the combined frustration from both intra-TSL and inter-TSL origins on the whole honeycomb structure. Here, J_{H3} plays a crucial role in suppressing the S phase. When the range of Z_2V phase broadens, J_{H3} mediates the inter-TSL geometrical frustration, and thus stabilizes the single- Z_2V state with a higher $|\kappa|$. (C_{nn} is positive but C_n and C_{nn} are negative in the Z_2V phase.)

It is noteworthy that the variation of RS from zero to one does not depend on VS monotonously. Figure 4(b) plots RS dependence on VS of all the Z_2V ground states. When VS is less than 420, RS equals 1. When VS is higher than 1152, RS approaches zero. But in the middle region, states with different RS exist at the same VS. The typical example is illustrated in Fig. 5. The first and second columns, respectively, plot the Z_2V ground states with RS=1 and 0.2222 for the same VS=648. The third and fourth columns, respectively, plot a pure single- Z_2V ground state with RS=1 and a pure triple- Z_2V metastable state with RS=0 at the same VS=288. The single- and triple- Z_2V features can be directly seen on the $v(r)$ map in Fig. 5. [The single- Z_2Vs in Fig. 5(g) are separated equidistantly [43]]. In the case of RS=1, $S'(\mathbf{k})$ in Figs. 5(b) and 5(h) presents the typical peaks similar to those observed in the triangular KH model [33], implying a modulation of the triangular superlattice originated from the approximately decoupled TSLs. Correspondingly $S\kappa'(\mathbf{k})$ of Figs. 5(c) and 5(i) shows the simple peaks similar to Fig. 3(f). In the case of RS=0.2222 and 0, $S'(\mathbf{k})$ and $S\kappa'(\mathbf{k})$ show the main peaks the same as the state of RS=1. However, besides main peaks, there are extra small peaks emerging on the hexagon's edges for $S'(\mathbf{k})$ and along some special lines for $S\kappa'(\mathbf{k})$ [Figs. 5(e), 5(f), 5(k), and 5(l)], which result from the extra hexangular character attached on the triangular superlattice in the honeycomb structure. This kind of triple- Z_2V state is only observed in the KH honeycomb model. Since Z_2Vs are topologically stable, extra energy is required to produce or remove Z_2Vs , namely, a potential barrier exists between the Z_2V states with different VS. But for the Z_2V states with the same VS, there is no potential barrier

between them, namely, one Z_2V state can reach another one with the same VS without energy consumption by just changing parameters at $T=0$. These topologically equivalent Z_2V states show triple- Z_2V dominant and single- Z_2V dominant features on different parameter points due to different frustration conditions. There may be an effective force between Z_2Vs , which is decided by the coupling parameters, but its distance dependence is too complex to be written into a simple expression due to multiple frustrations.

Since the Z_2Vs are calculated on one TSL as mentioned above, an interesting question remains, that is, how the Z_2Vs on two TSLs are arranged in the whole honeycomb structure. The simulation reveals that they are arranged in different styles for the single- Z_2V and triple- Z_2V states. In the case of the single- Z_2V state, the single- Z_2Vs emerge as typical κ vortices on $(1,1,1)$, $(1,-1,-1)$, $(-1,1,-1)$, and $(-1,-1,1)$ planes (marked as 1, 2, 3, and 4), forming a triangular lattice on each TSL as illustrated in Fig. 6(a). If these single- Z_2Vs on two TSLs are plotted into one picture as given in Fig. 6(b), these two single- Z_2V triangular lattices interpenetrate into each other to construct a honeycomb lattice in the manner that each single- Z_2V has three neighbors on different planes. On the other hand, in the case of the triple- Z_2V state, the $\kappa(r)$ map on one TSL shows hexagonal domain structure, where κ domains along $[1,1,1]$ (or $[-1,-1,-1]$), $[1,-1,-1]$ (or $[-1,1,1]$), $[-1,1,-1]$ (or $[1,-1,1]$), and $[-1,-1,1]$ (or $[1,1,-1]$) are marked as 1, 2, 3, and 4. The Z_2V triples appearing on the intersection of six domains of three types are also marked as 1, 2, 3, and 4 in the form of Fig. 6(e), i.e., they are named after the type of κ domain that does not appear around this Z_2V triple. These Z_2V triples construct a triangular lattice on each TSL. If $\kappa(r)$ maps on two TSLs are plotted into one picture as illustrated in Fig. 6(f), the Z_2V triples of the same type from two TSLs nearly overlap with each other, and moreover the κ domains of the same type and nearly opposite orientations also overlap with each other. Although $\kappa(r)$ and $\nu(r)$ maps are calculated on one TSL, they demonstrate the nontrivial modulation actually existing on the whole honeycomb structure. As plotted in Figs. 6(c) and 6(g), the site-dependent local energy $E_i(r)$ of the honeycomb structure just displays the pattern corresponding to the $\kappa(r)$ map including two TSLs. All these nontrivial properties finally come from the modulation of spin configuration on the whole honeycomb structure, which presents a very complex superlattice pattern as plotted in Figs. 6(d) and 6(h).

IV. CONCLUSION

In summary, the Z_2V phase is well located and systematically investigated by simulation in the KH honeycomb model expanded by considering J_{H2} and J_{H3} . In the region of the Z_2V phase, a gradual modulation of vortex density is observed, together with a transition from single- Z_2V to triple- Z_2V state driven by the variation of frustration condition. The triple- Z_2V state is induced by the frustration from both intra-TSL and inter-TSL origins on the whole honeycomb structure, while the single- Z_2V state mostly results from the frustration within one TSL. Topologically equivalent states with the same VS, showing the single- Z_2V dominant and the triple- Z_2V dominant features on different parameter points, can be controlled by the frustration condition to switch between each other without energy consumption. For the whole honeycomb structure, the Z_2Vs are arranged in different styles, namely, interpenetrating for the single- Z_2V state and overlapping for the triple- Z_2V state. It is worth noting that J_{H3} is a crucial factor to the Z_2V phase in this system. It plays a key role in

expanding and stabilizing the Z_2V phase. Moreover it mediates the inter-TSL geometrical frustration and thus modulates the single- Z_2V state.

References:

- [1] A. A. Abrikosov, *Sov. Phys. JETP* **5**, 1174 (1957).
- [2] G. Blatter, M. V. Feigelman, V. B. Geshkenbein, A. I. Larkin, and V. M. Vinokur, *Rev. Mod. Phys.* **66**, 1125 (1994).
- [3] T. Choi, Y. Horibe, H. T. Yi, Y. J. Choi, W. Wu, and S.-W. Cheong, *Nature Mater.* **9**, 253 (2010).
- [4] S. C. Chae, Y. Horibe, D. Y. Jeong, S. Rodan, N. Lee, and S.-W. Cheong, *PNAS* **107**, 21366 (2010).
- [5] S. M. Griffin, M. Lilienblum, K. T. Delaney, Y. Kumagai, M. Fiebig, and N. A. Spaldin, *Phys. Rev. X* **2**, 041022 (2012).
- [6] M.-G. Han, Y. Zhu, L. Wu, T. Aoki, V. Volkov, X. Wang, S. C. Chae, Y. S. Oh, and S.-W. Cheong, *Adv. Mater.* **25**, 2415 (2013).
- [7] X. Wang, M. Mostovoy, M. G. Han, Y. Horibe, T. Aoki, Y. Zhu, and S.-W. Cheong, *Phys. Rev. Lett.* **112**, 247601 (2014).
- [8] J. M. Kosterlitz and D. J. Thouless, *J. Phys. C* **6**, 1181 (1973).
- [9] H. Kawamura and M. Kikuchi, *Phys. Rev. B* **47**, 1134(R) (1993).
- [10] H. Kawamura and S. Miyashita, *J. Phys. Soc. Jpn.* **53**, 4138 (1984).
- [11] T. Okubo and H. Kawamura, *J. Phys. Soc. Jpn.* **79**, 084706 (2010).
- [12] H. Kawamura, A. Yamamoto, and T. Okubo, *J. Phys. Soc. Jpn.* **79**, 023701 (2010).
- [13] R. Tamura, S. Tanaka, and N. Kawashima, *Phys. Rev. B* **87**, 214401 (2013).
- [14] J. Chaloupka, G. Jackeli, and G. Khaliullin, *Phys. Rev. Lett.* **105**, 027204 (2010).
- [15] J. Reuther, R. Thomale, and S. Trebst, *Phys. Rev. B* **84**, 100406 (2011).
- [16] H.-C. Jiang, Z.-C. Gu, X.-L. Qi, and S. Trebst, *Phys. Rev. B* **83**, 245104 (2011).
- [17] J. Reuther, R. Thomale, and S. Rachel, *Phys. Rev. B* **90**, 100405 (2014).
- [18] J. Chaloupka, G. Jackeli, and G. Khaliullin, *Phys. Rev. Lett.* **110**, 097204 (2013).
- [19] C. Price and N. B. Perkins, *Phys. Rev. B* **88**, 024410 (2013).
- [20] Y. Singh, S. Manni, J. Reuther, T. Berlijn, R. Thomale, W. Ku, S. Trebst, and P. Gegenwart, *Phys. Rev. Lett.* **108**, 127203 (2012).
- [21] J. G. Rau, Eric Kin-Ho Lee, and H.-Y. Kee, *Phys. Rev. Lett.* **112**, 077204 (2014).
- [22] L. Janssen, E. C. Andrade, and M. Vojta, *Phys. Rev. Lett.* **117**, 277202 (2016).
- [23] K. W. Plumb, J. P. Clancy, L. J. Sandilands, V. V. Shankar, Y. F. Hu, K. S. Burch, H.-Y. Kee, and Y.-J. Kim, *Phys. Rev. B* **90**, 041112 (2014).
- [24] J. Chaloupka and G. Khaliullin, *Phys. Rev. B* **94**, 064435 (2016).
- [25] Y. Sizyuk, P. Wolfle, and N. B. Perkins, *Phys. Rev. B* **94**, 085109 (2016).
- [26] R. D. Johnson, S. C. Williams, A. A. Haghighirad, J. Singleton, V. Zapf, P. Manuel, I. I. Mazin, Y. Li, H. O. Jeschke, R. Valentí, and R. Coldea, *Phys. Rev. B* **92**, 235119 (2015).
- [27] H. B. Cao, A. Banerjee, J.-Q. Yan, C. A. Bridges, M. D. Lumsden, D. G. Mandrus, D. A. Tennant, B. C. Chakoumakos, and S. E. Nagler, *Phys. Rev. B* **93**, 134423 (2016).
- [28] A. Banerjee, C. A. Bridges, J.-Q. Yan, A. A. Aczel, L. Li, M. B. Stone, G. E. Granroth, M. D. Lumsden, Y. Yiu, J. Knolle, S. Bhattacharjee, D. L. Kovrizhin, R. Moessner, D. A. Tennant, D. G. Mandrus, and S. E. Nagler, *Nature Mater.* **15**, 733 (2016).
- [29] K. Ran, J. Wang, W. Wang, Z.-Y. Dong, X. Ren, S. Bao, S. Li, Z. Ma, Y. Gan, Y. Zhang,

- J. T. Park, G. Deng, S. Danilkin, S.-L. Yu, J.-X. Li, and J. Wen, Phys. Rev. Lett. **118**, 107203 (2017).
- [30] A. Glamazda, P. Lemmens, S.-H. Do, Y. S. Kwon, and K.-Y. Choi, Phys. Rev. B **95**, 174429 (2017).
- [31] I. Kimchi and Y.-Z. You, Phys. Rev. B **84**, 180407 (2011).
- [32] Y. Sizyuk, C. Price, P. Wolfle, and N. B. Perkins, Phys. Rev. B **90**, 155126 (2014).
- [33] I. Rousochatzakis, U. K. Rossler, J. van en. Brink, and M. Daghofer, Phys. Rev. B **93**, 104417 (2016).
- [34] M. Becker, M. Hermanns, B. Bauer, M. Garst, and S. Trebst, Phys. Rev. B **91**, 155135 (2015).
- [35] X. Yao and S. Dong, Scientific Reports **6**, 26750 (2016).
- [36] M. Creutz, Phys. Rev. D **36**, 515 (1987).
- [37] L. W. Lee and A. P. Young, Phys. Rev. B **76**, 024405 (2007).
- [38] L. Messio, C. Lhuillier, and G. Misguich, Phys. Rev. B **83**, 184401 (2011).
- [39] I. Rousochatzakis, J. Reuther, R. Thomale, S. Rachel, and N. B. Perkins, Phys. Rev. X **5**, 041035 (2015).
- [40] X. Liu, T. Berlijn, W.-G. Yin, W. Ku, A. Tselik, Y.-J. Kim, H. Gretarsson, Y. Singh, P. Gegenwart, and J. P. Hill, Phys. Rev. B **83**, 220403 (2011).
- [41] S. K. Choi, R. Coldea, A. N. Kolmogorov, T. Lancaster, I. I. Mazin, S. J. Blundell, P. G. Radaelli, Y. Singh, P. Gegenwart, K. R. Choi, S.-W. Cheong, P. J. Baker, C. Stock, and J. Taylor, Phys. Rev. Lett. **108**, 127204 (2012).
- [42] F. Ye, S. Chi, H. Cao, B. C. Chakoumakos, J. A. Fernandez-Baca, R. Custelcean, T. F. Qi, O. B. Korneta, and G. Cao, Phys. Rev. B **85**, 180403 (2012).
- [43] See Supplemental Material.

Acknowledgments

This work is supported by research grants from the National Natural Science Foundation of China (Grant Nos. 11674055). We thank Prof. Maria Daghofer for helpful discussions.

Figure Legends:

FIG. 1. (a) A sketch of the honeycomb lattice, which is composed of two TSLs as represented by white and gray dots, respectively. The solid, dashed, and dotted black thick lines indicate three kinds of spin-dependent nearest-neighbor bonds, where xx , yy and zz involve S^x , S^y , and S^z , respectively. The vector chirality ($\boldsymbol{\kappa}$) is calculated on the shading downward-pointing elementary triangles of one TSL. The vorticity (ν) is evaluated on right- and left-pointing triangular loops connecting one-third downward-pointing triangles with darker shading. (b) Partial $\boldsymbol{\kappa}(r)$ map, where the arrows present the projections of $\boldsymbol{\kappa}$ onto the (111) plane, and the color refers to the value of $|\boldsymbol{\kappa}|$. (c) Partial $\nu(r)$ map with one Z_2V calculated on the $\boldsymbol{\kappa}(r)$ configuration of (b), where the yellow dot represents $\nu=1$ and the black one denotes $\nu=0$.

FIG. 2. The phase diagram in the space of φ and J_{H2} for (a) $J_{H3}=0$, (b) $J_{H3}=0.1$, (c) $J_{H3}=0.15$, and (d) $J_{H3}=0.2$, and in the space of φ and J_{H3} for (e) $J_{H2}=0.2$, (f) $J_{H2}=0.3$, (g) $J_{H2}=0.4$, and (h) $J_{H2}=0.5$. The solid squares filled with different colors show the ground states identified as the commensurate ordered phases, and those empty squares represent the unidentified regions. The large solid circles show Z_2V ground states, and the solid small circles on colorful squares show Z_2V metastable states, where the shading refers to the value of VS. The shading of the small filled triangles on the circles refers to the value of RS.

FIG. 3. (a) Partial map of $\nu(r)$, (b) $S^y(\mathbf{k})$, and (c) $S\kappa^z(\mathbf{k})$ in the ground state of VS=1152 obtained with $J_{H2}=0.3$, $J_{H3}=0.05$, and $\varphi=1.65625\pi$. (d) Partial map of $\nu(r)$, (e) $S^y(\mathbf{k})$, and (f) $S\kappa^z(\mathbf{k})$ in the ground state of VS=72 obtained at $J_{H2}=0.3$, $J_{H3}=0.3$, and $\varphi=1.84375\pi$. For the $\nu(r)$ map, the yellow dot represents $\nu=1$ and the black one denotes $\nu=0$. For $S^y(\mathbf{k})$ and $S\kappa^z(\mathbf{k})$, the solid, dashed and dotted lines with arrows denote the signals from x , y and z components, respectively.

FIG. 4. (a) $|k_p|$ and $|kk_p|$ as functions of VS with error bars. (b) The dependence of RS on VS. (c,d) The Z_2V phase area of Fig. 2(b) with $J_{H3}=0.1$. (e,f) The Z_2V phase area of Fig. 2(g) with $J_{H2}=0.4$. (c,e) The shading of the left-half dot refers to the value of $|C_n|$ from 0.280(white) to 0.872(dark), and that of the right half refers to the value of $|C_{nnn}|$ from 0.350(white) to 2.350(dark). (d,f) The shading of the left-half dot refers to the value of $|C_{nn}|$ from 2.188(white) to 2.692(dark), and that of the right half refers to the averaged value of $|\boldsymbol{\kappa}|$ from 0.759(white) to 0.905(dark).

FIG. 5. Partial $\nu(r)$ map, $S^y(\mathbf{k})$, and $S\kappa^z(\mathbf{k})$ are displayed in the first, second, and third rows. The first column gives the ground state with VS=648 and RS=1 obtained at $J_{H2}=0.45$, $J_{H3}=0.15$ and $\varphi=1.84375\pi$. The second column shows the ground state with VS=648 and RS=0.22222 obtained at $J_{H2}=0.5$, $J_{H3}=0.0$ and $\varphi=1.65625\pi$. The third column gives the ground state with VS=288 and RS=1 obtained at $J_{H2}=0.2$, $J_{H3}=0.2$ and $\varphi=1.75\pi$. The fourth column presents the metastable state with VS=288 and RS=0 obtained at $J_{H2}=0.45$, $J_{H3}=0.0$ and $\varphi=1.625\pi$. For the $\nu(r)$ map, the yellow dot represents $\nu=1$ and the black one denotes $\nu=0$. For $S^y(\mathbf{k})$ and $S\kappa^z(\mathbf{k})$, the solid, dashed, and dotted lines with arrows denote the signals from x ,

y, and z components, respectively.

FIG. 6. The first row displays the single- Z_2V ground state with $VS=72$ and $RS=1$ obtained at $J_{H2}=0.3$, $J_{H3}=0.3$, and $\varphi=1.84375\pi$. The second row shows the triple- Z_2V metastable state with $VS=288$ and $RS=0$ obtained at $J_{H2}=0.45$, $J_{H3}=0.0$, and $\varphi=1.625\pi$. The first column presents the $\kappa(r)$ map on one TSL. The second column displays the $\kappa(r)$ map with all κ vectors from two TSLs. (See Supplemental Material for details [43].) The arrows present the projections of κ onto the (111) plane, and the color refers to the value of $|\kappa|$. The single- Z_2Vs are marked as 1, 2, 3 and 4 written on solid circles in (a). In (b), besides the Z_2Vs from (a), the single- Z_2Vs from another TSL are also marked in the same manner as 1, 2, 3, and 4 written on solid rectangles. For (e) and (f), κ domains are marked as 1, 2, 3, and 4. The Z_2V triples are marked as 1, 2, 3, and 4 written on solid circles. The third column exhibits the $E_i(r)$ map of the honeycomb structure, and the shading refers to the value of E_i . The fourth column plots the spin configuration of the honeycomb structure. The vectors show the projections of spins onto the (111) plane with the shading referring to the component of spin perpendicular to the (111) plane. For visibility, only part of the lattice is plotted.

Table I. The standard values of the correlation functions C_n , C_{nn} , C_{nnn} , and C_K for F, N, S, Z, and D phases.

	F	N	S	Z	D
C_n	3	-3	-1	1	0
C_{nn}	6	6	-2	-2	-3
C_{nnn}	3	-3	3	-3	0
C_K	1	-1	1	1	1

Fig. 1

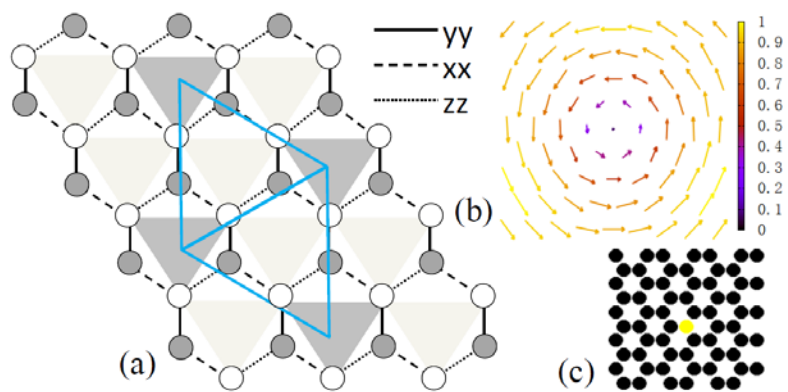


Fig. 2

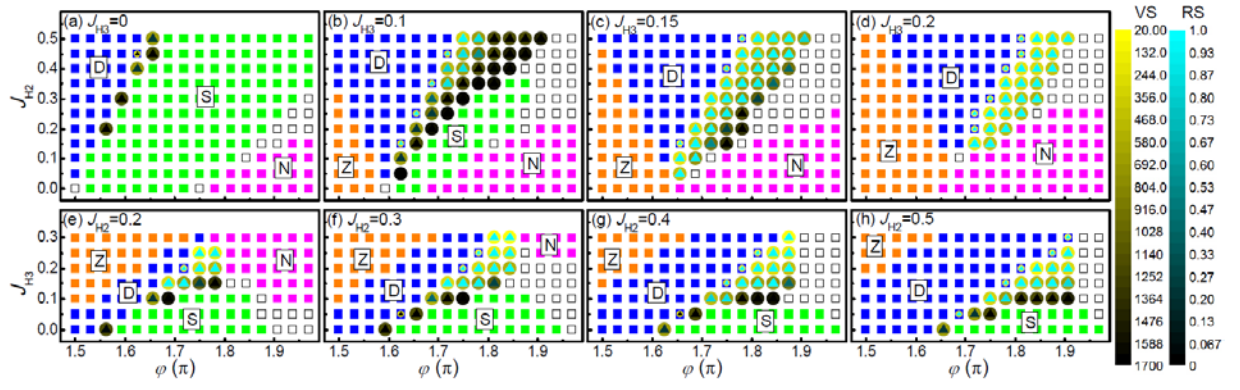


Fig. 3

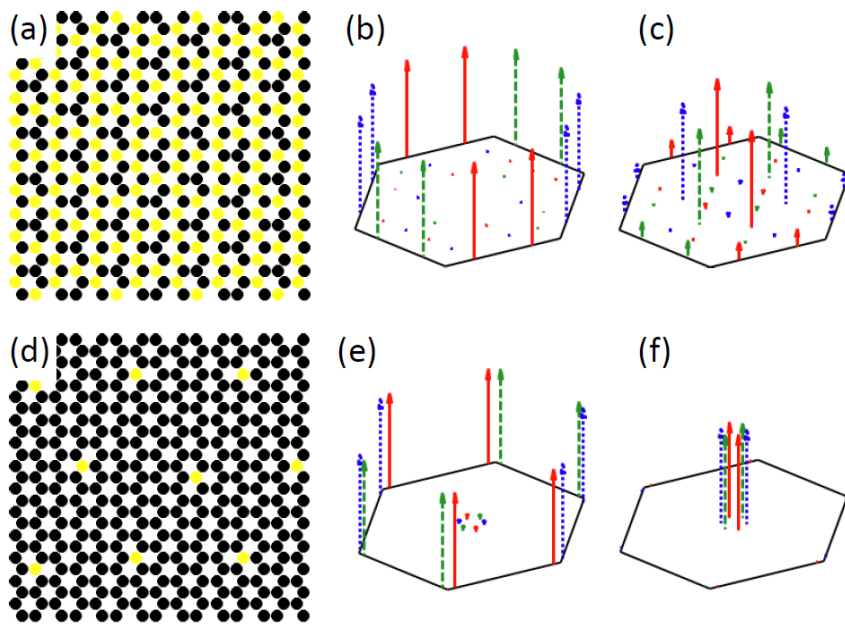


Fig. 4

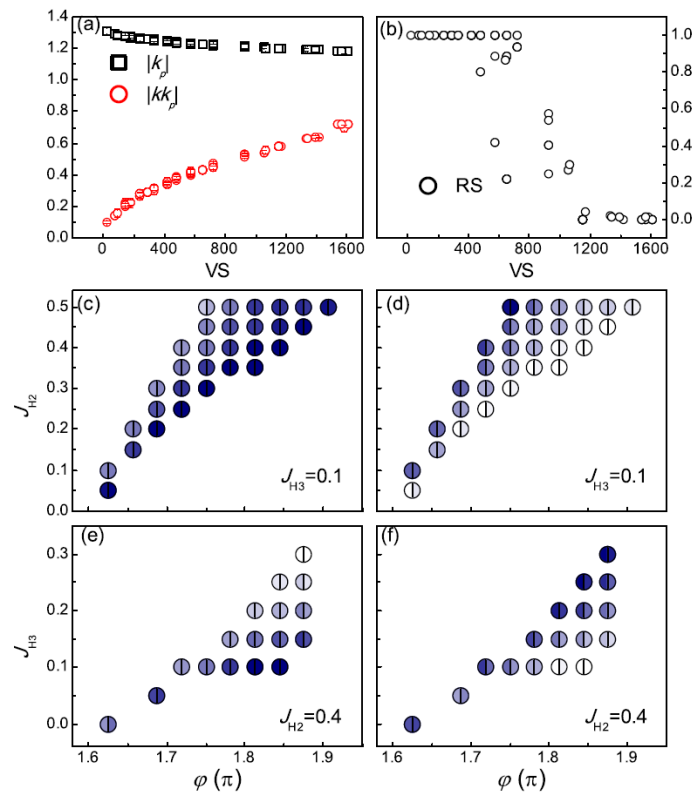


Fig. 5

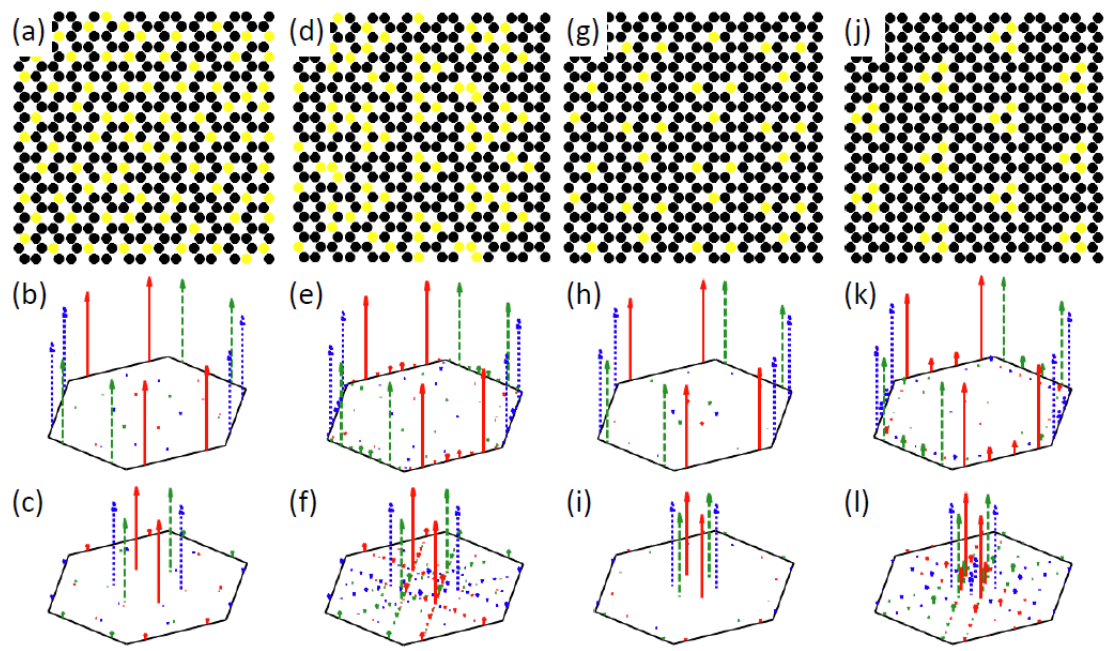


Fig. 6

